Application of the virtual fields method to large strain anisotropic plasticity

Marco Rossi[a], Fabrice Pierron[b], Michaela Štamborská[c]

[a] Dipartimento di Ingegneria Industriale e Scienze Matematiche, Università Politecnica delle Marche, Monte Dago, via Brecce Bianche, 60131 Ancona, Italy,
email: m.rossi@univpm.it
[b]Engineering and the Environment, University of Southampton, Highfield, Southampton SO17 1BJ, UK, email: f.pierron@soton.ac.uk
[c]Institute of Materials & Machine Mechanics Slovak Academy of Sciences, Račianska 75, 831 02 Bratislava, Slovakia

---

Abstract

The identification of the plastic behaviour of sheet metals at severe deformation is extremely important for many industrial application such as metal forming, crashworthiness, automotive, aerospace, piping, etc. In this paper, the virtual fields method (VFM) was employed to identify the constitutive parameters of anisotropic plasticity models. The method was applied using the finite deformation theory in order to account for large strains. First the theoretical principles to implement the method are described in details, especially how to derive the stress field from the strain field. Afterwards a numerical validation was performed using the Hill48 model. Several aspects were studied with the numerical model: the effect of the used virtual fields, the minimum number of specimens required to identify the parameters, the stress distribution obtained from the specimen and its influence in the identification performance. A brief analysis on the influence of noise is also conducted. Finally a series of experiments was conducted on notched

Preprint submitted to International Journal of Solids and Structures June 30, 2016

specimens of stainless steel, cut along different anisotropic directions. The displacement and strain fields were obtained by digital image correlation. Afterwards, the VFM was used to identify the parameters of the Hill48 model and the Yld2000-2D model. In this case, the Hill48 model was not able to correctly describe the material behaviour, while a rather good agreement was found with the Yld2000-2D model. The potential and the limitation of the proposed method are finally discussed.

Keywords:

Anisotropic plasticity, inverse identification, large strains, full-field measurements, virtual fields method

---

1. Introduction

Nowadays, most metal forming operations are designed with the aid of finite element (FE) models. However, in order to have reliable predictions, the computations have to be fed with suitable constitutive models that describe the mechanical behaviour of the material at the meso-scale level.

In particular, sheet metals often exhibit anisotropic behaviour when they undergo plastic deformation, this is mainly due to the rolling process adopted to manufacture the blank sheets, which introduces anisotropy in the metal texture. This effect has significant influence on sheet metal forming processes and has to be accurately taken into consideration in order to have reliable outcomes from FE simulations.

The first step in this direction is the choice of the constitutive model. Many models for anisotropic plasticity have been developed and described in the literature, although only few of them are actually used by industry, which tends to prefer simple models implemented in commercial FE codes. Among them, the Hill48 model (Hill, 1948) is still one of the most used and is implemented in almost every commercial FE code. The main limitation of the Hill48 model is that there is a fixed relation between the yield stress and Lankford parameter R in different directions. A popular model, which overtakes the main limitations of Hill48, is Yld2000-2D proposed by Barlat et al. (2003) and Yoon et al. (2004). Furthermore, Vegter and Van Den Boogaard (2006) use Bézier curves to describe the yield locus. Cazacu et al. (2006) extended the work of Barlat et al. (1991) to hexagonal close packed metals. Examples of models that take into account the Lode's angle dependency have been presented by Bai and Wierzbicki (2008) and Cortese et al. (2014). Other interesting contributions have been given by Darrieulat and Piot (1996), Feigenbaum and Dafalias (2007) and many other examples could be provided.

Once the constitutive model is selected, the next step is to identify the corresponding material parameters from experiments. This calibration is essential to have reliable results. Usually the experiments consist in simple uniaxial tests where the state of stress within the specimen is well known and can be simply deduced from the measured force.

Recently, however, strategies based on full-field measurements and inverse methods have seen significant growth (Grédiac et al., 2012). In this case, a specimen with a non-regular geometry is tested, the displacement field is measured with a full-field technique (e.g digital image correlation, grid method) and used to identify the material parameters. The advantage is that, from a single test, many different stress-strain conditions can be investigated at the same time.

The inverse identification can be carried out by finite element model updating (FEMU), i.e. the experimental measurements are compared with that obtained from an FE model of the same test and the material parameters are iteratively updated in order to obtain the best fit between numerical and experimental results. Many applications of FEMU to plasticity have been reported in the literature. To give a brief overlook, Kajberg and Lindkvist (2004) applied FEMU to large strain plasticity, Lecompte et al. (2007), Cooreman et al. (2008) and Teaca et al. (2010) used biaxial tests and DIC to identify the anisotropic behaviour of sheet metals, Güner et al. (2012) used a FEMU approach to calibrate the Yld2000-2D parameters, showing the convenience of including full-field measurement in the cost function.

On the other hand, several inverse techniques do not require the use of FE to perform the inverse identification. For instance Coppieters et al. (2011) and Coppieters and Kuwabara (2014) used a cost function based on the comparison of the internal and external work. Rossi et al. (2008) used the equilibrium of transverse sections of the specimen. Among those approaches, the virtual fields method (VFM) is one of the most used and widespread (Pierron and Grédiac, 2012).

The application of the VFM to plasticity was firstly addressed by Grédiac and Pierron (2006), Pannier et al. (2006) and Avril et al. (2008). Then many other applications have been presented, for instance Le Louëdec et al. (2013) applied the VFM to the elasto-plastic behaviour of welded materials, Pierron et al. (2010) investigated cyclic loads and kinematic hardening, Kim et al. (2013) look at the post-necking strain hardening behaviour.

The first application of VFM to anisotropic plasticity was published by Rossi and Pierron (2012a), where a complete three-dimensional framework for large strain plasticity is presented, an application to planar anisotropy was then developed by Kim et al. (2014) using Σ-shaped specimens.

In this paper, an application of the VFM to anisotropic plasticity at large strain is presented, with the intent of investigating several aspects that characterize this specific inverse problem and that were not yet evaluated in the previous studies. In particular, the main novelties introduced in this paper are

- the VFM is adapted to large strains and a direct stress reconstruction algorithm is used that allows to reduce the computational time;
- the influence of the stress state on the identification is studied in detail using a normalized stress plane, which permits to verify which zones of the yielding surface are covered by the experiments;
- the influence of noise, different virtual fields, and specimen orientation is evaluated;
- the Yld2000-2D model is implemented and used to identify the plastic behaviour on experimental data,

The paper is organized as follows: Section 2 describes the theoretical model and the implementation of the Hill48 and Yld2000-2D criteria, Section 3 presents a numerical validation using Hill48 as reference, Section 4 describes the experiments performed on a stainless steel sheet metal and Section 5 illustrates and discusses the results of the VFM identification on the experiments using both Hill48 and Yld2000-2D.

2. Theoretical model

The VFM is employed here to identify the parameters of an anisotropic plasticity model at large strain. The same procedure as described by Rossi and Pierron (2012a) for a general three-dimensional case is adapted to the plane stress case, using the Hill48 yield criterion.

2.1. The non-linear VFM at large strains

The VFM relies on the principle of virtual work which is an integral form of mechanical equilibrium. In finite deformation, there is a distinction between the reference placement $\mathscr{B}_0$ of the body and its current placement $\mathscr{B}_t$ at time t. Let us consider an arbitrary continuous and differentiable vectorial field $\delta\mathbf{v}$. In absence of body forces and acceleration, the principle of virtual work, in the current placement, can be written as:

$$\int_{\mathscr{B}_t} \mathbf{T} \colon \delta\mathbf{D}\, dv = \int_{\partial\mathscr{B}_t} \mathbf{t} \cdot \delta\mathbf{v}\, da \tag{1}$$

where $\mathbf{T}$ is the Cauchy stress tensor, $\mathbf{t}$ is the stress vector at the boundary of the solid, in the current placement, dv and da are the infinitesimal elements of volume and area in the current placement $\mathscr{B}_t$ and $\delta\mathbf{D}$ is defined as[1]:

$$\delta\mathbf{D} = \tfrac{1}{2}\left(grad\ \delta\mathbf{v} + grad^T\ \delta\mathbf{v}\right) \tag{2}$$

The integrals of Eq. 1 are computed in the current placement $\mathscr{B}_t$, using an Eulerian or spatial description. However, the same equation can be rewrit-

---

[1] at large strains, the principle of virtual work is sometimes named principle of virtual power because $\delta\mathbf{v}$ can be viewed as a virtual velocity field and $\delta\mathbf{D}$ as a virtual stretch rate tensor.

ten in terms of the reference placement $\mathscr{B}_0$ using a Lagrangian or material description. It follows:

$$\int_{\mathscr{B}_0} \mathbf{T}^{1PK} : \delta\mathbf{F}^{\bullet} \, dv_0 = \int_{\partial\mathscr{B}_0} \left(\mathbf{T}^{1PK}\mathbf{n}_0\right) \cdot \delta\mathbf{v} \, da_0 \tag{3}$$

where $\mathbf{T}^{1PK}$ is the 1st Piola-Kirchhoff stress tensor, defined as:

$$\mathbf{T}^{1PK} = det\left(\mathbf{F}\right)\mathbf{T}\,\mathbf{F}^{-T} \tag{4}$$

and $\delta\mathbf{F}^{\bullet}$ is the gradient of $\delta\mathbf{v}$ in the Lagrangian description:

$$\delta\mathbf{F}^{\bullet} = Grad\,\delta\mathbf{v}\left(\mathbf{x}_0, t\right) \tag{5}$$

Eq. 1 and Eq. 3 are mathematically equivalent and have to be satisfied at each time t of the test. In this application, the Lagrangian description is more convenient, because it allows writing the virtual field $\delta\mathbf{v}$ in the undeformed configuration and it will be adopted accordingly.

Let us now consider a general plasticity model governed by N_{cp} constitutive parameters and call $\boldsymbol{\xi} = \left\{X_1, X_2, \ldots, X_{N_{cp}}\right\}$ the vector of such parameters. The constitutive model links the stress field to the strain field, which, in turn, is derived from the displacement field $\boldsymbol{u}$. Therefore, the stress field at time t is a function of $\boldsymbol{\xi}$ and $\boldsymbol{u}$:

$$\mathbf{T} = \mathbf{T}\left(\boldsymbol{\xi}, \boldsymbol{u}|_{0\rightarrow t}\right) \tag{6}$$

Since plasticity is a path dependent process, the whole displacement history of $\boldsymbol{u}$, from time 0 to t, has to be considered, as specified in Eq. 6. In inverse problems, the displacement history is known from the experiments while the constitutive parameters have to be identified. To this purpose the following function can be defined:

$$\psi\left(\boldsymbol{\xi}, \delta\mathbf{v}, t\right) = \left| \int_{\mathscr{B}_0} \mathbf{T}^{1PK} \cdot \delta\mathbf{F}^{\bullet} \, dv_0 - \int_{\partial\mathscr{B}_0} \left(\mathbf{T}^{1PK}\mathbf{n}_0\right) \cdot \delta\mathbf{v} \, da_0 \right| \tag{7}$$

According to the principle of virtual work stated in Eq. 3, the function ψ has to be zero for any admissible virtual fields $\delta\mathbf{v}$, at any time t of the test. Considering N_v admissible virtual fields and N_t time steps of the test, a general cost function can be written in terms of the constitutive parameters $\boldsymbol{\xi}$:

$$\Psi\left(\boldsymbol{\xi}\right) = \frac{1}{N_v N_t} \sum_{i=1}^{N_v} \sum_{j=1}^{N_t} \psi\left(\boldsymbol{\xi}, \delta\mathbf{v}_i, t_j\right) \tag{8}$$

The non-linear VFM consists in the minimization of Eq. 8. This allows finding out the parameters that best satisfy the equilibrium law, written in the form of the principle of virtual work. Key elements for the success of the non-linear VFM are the procedure to evaluate the stress field from the measured displacement field and the choice of virtual fields. These aspects will be covered in the next sections.

2.2. Computation of stress from the displacement field

The stress field is computed starting from the displacement field, which is measured by experiments. Different algorithms can be used to this purpose. For instance, Kim et al. (2013) used the measured displacement field to determine the nodal displacement of a triangular mesh generated over the area of measurements, then the problem is handled using the same relations as in FE with prescribed nodal displacements.

In this paper, the procedure described by Rossi and Pierron (2012a) has been used, adapted to the plane stress condition and the Hill48 yield criterion. The idea is that the stress field at time t can be derived directly from the direction of the plastic flow and the cumulated equivalent plastic strain. This approach is easy to implement and can be readily adapted to other constitutive models.

A generic yield criterion is defined as a function of the Cauchy stress $\mathbf{T}$:

$$\Phi_p\left(\mathbf{T}\right) = \sigma_T\left(\mathbf{T}\right) - \sigma_Y = 0 \tag{9}$$

where σ_T is the equivalent stress, a scalar function of the current stress state $\mathbf{T}$, and σ_Y is the yield stress, identified as the yield limit in a uniaxial tensile test in a certain material direction. According to the Hill48 model, the equivalent stress function writes:

$$\begin{aligned}\sigma_T\left(\mathbf{T}\right) = \big[f\left(\sigma_{22}-\sigma_{33}\right)^2 + g\left(\sigma_{33}-\sigma_{11}\right)^2 +& \\ h\left(\sigma_{11}-\sigma_{22}\right)^2 + 2l\;\sigma_{23}^2 + 2m\;\sigma_{31}^2 + 2n\;\sigma_{12}^2\big]^{\frac{1}{2}}&\end{aligned} \tag{10}$$

where σ_{ij} are the components of $\mathbf{T}$ written in a coordinate system oriented to the anisotropic axes (see Figure 1), and f, g, h, l, m, n are constants which describe the anisotropic behaviour. In plane stress condition ($\sigma_{33} = \sigma_{13} = \sigma_{31} = 0$), Eq. 10 reduces to:

$$\sigma_T\left(\mathbf{T}\right) = \left[\left(g+h\right)\sigma_{11}^2 + \left(f+h\right)\sigma_{22}^2 - 2h\;\sigma_{11}\sigma_{22} + 2n\;\sigma_{12}^2\right]^{\frac{1}{2}} \tag{11}$$

The four anisotropic constants of Eq. 11 can be obtained as a function of the Lankford parameter R (Lankford et al., 1950), measured in three different orientations. R is the ratio of the transverse to the through thickness strain in a uniaxial tensile test. Accordingly, the anisotropic parameters can be obtained as follow (Banabic et al., 2000):

$$f=\frac{R_0}{(1+R_0)R_{90}};\ g=\frac{1}{1+R_0};\ h=\frac{R_0}{1+R_0};\ n=\left(\frac{1}{2}+R_{45}\right)\left(1+\frac{R_0}{R_{90}}\right); \tag{12}$$

with R evaluated at 0°, 45° and 90° with respect to the first anisotropic direction, which is usually the rolling one in sheet metals. From the yield criterion, using an associative flow rule, the direction of the plastic flow is deduced as:

$$\widehat{\mathbf{N}}_p=\frac{\mathrm{d}\,\Phi_p\left(\mathbf{T}\right)}{\mathrm{d}\,\mathbf{T}}\Bigg/\left|\frac{\mathrm{d}\,\Phi_p\left(\mathbf{T}\right)}{\mathrm{d}\,\mathbf{T}}\right| \tag{13}$$

where $\widehat{\mathbf{N}}_p=\left\{\widehat{n}^p_{ij}\right\}$ is the versor which indicates the direction of the plastic flow. Let us now rewrite the stress tensor $\mathbf{T}$ in terms of the versor $\widehat{\mathbf{N}}_T=\left\{\widehat{n}^T_{ij}\right\}$ that defines the "direction"of the stress tensor:

$$\mathbf{T}=\left|\mathbf{T}\right|\widehat{\mathbf{N}}_T \tag{14}$$

From Eq. 11, Eq. 13 and Eq. 14, the direction of the plastic flow for Hill48 becomes:

$$\frac{\mathrm{d}\,\Phi_p\left(\mathbf{T}\right)}{\mathrm{d}\,\mathbf{T}}=\sigma_T^{-\frac{1}{2}}\begin{bmatrix}(h+g) & -h & 0\\ -h & (f+h) & 0\\ 0 & 0 & 2n\end{bmatrix}\begin{Bmatrix}\widehat{n}^T_{11}\\ \widehat{n}^T_{22}\\ \widehat{n}^T_{12}\end{Bmatrix} \tag{15}$$

this relation can be inverted to obtain the direction of the stress tensor:

$$\widehat{\mathbf{N}}_T = \frac{\boldsymbol{\mathsf{A}}\,\widehat{\mathbf{N}}_p}{\left|\boldsymbol{\mathsf{A}}\,\widehat{\mathbf{N}}_p\right|} \tag{16}$$

with

$$\boldsymbol{\mathsf{A}}\,\widehat{\mathbf{N}}_p = \begin{bmatrix} f+h & h & 0 \\ h & h+g & 0 \\ 0 & 0 & \frac{gf+gh+hf}{2n} \end{bmatrix} \begin{Bmatrix} \widehat{n}^P_{11} \\ \widehat{n}^P_{22} \\ \widehat{n}^P_{12} \end{Bmatrix} \tag{17}$$

The versor of the stress tensor $\widehat{\mathbf{N}}_T$ is directly derived from the direction of the plastic flow $\widehat{\mathbf{N}}_p$. The modulus of the stress tensor $|\mathbf{T}|$ from the versor $\widehat{\mathbf{N}}_T$ can also be computed. Indeed, from Eq. 9 and Eq. 11:

$$\sigma_T\left(\mathbf{T}\right) = \sigma_T\left(|\mathbf{T}|\,\widehat{\mathbf{N}}_T\right) = |\mathbf{T}|\,\sigma_T\left(\widehat{\mathbf{N}}_T\right) = \sigma_Y \tag{18}$$

and:

$$|\mathbf{T}| = \sigma_Y\left[\left(g+h\right)\widehat{n}^T_{11}{}^2 + \left(f+h\right)\widehat{n}^T_{22}{}^2 - 2h\,\widehat{n}^T_{11}\widehat{n}^T_{22} + 2n\;\widehat{n}^T_{12}{}^2\right]^{-\frac{1}{2}} \tag{19}$$

Then stress tensor $\mathbf{T}$ is obtained from Eq. 14.

The yield stress σ_Y depends on the hardening law, which is usually a function of the equivalent plastic strain. The procedure above, applied to the Hill48 yield function, is general and can be adapted to any plasticity model with a convex yield locus. For more in-depth insight on this, the reader is referred to Rossi and Pierron (2012a).

The hardening law used here is Swift's law expressed by:

$$\sigma_Y = K_H\left(p+\varepsilon_0\right)^{N_H} \tag{20}$$

where σ_Y is the yield stress, K_H, ε_0 and N_H are the model parameters, and p is the equivalent cumulated plastic strain. The equivalent plastic strain is defined so that the plastic work can be expressed in terms of the equivalent stress, that is:

$$\int_{p(0)}^{p(t)} \sigma_Y dp = \int_{\mathbf{E}^p(0)}^{\mathbf{E}^p(t)} \mathbf{T} : d\mathbf{E}^p \tag{21}$$

where $\mathbf{E}^p$ is the plastic strain tensor. Combining Eq. 9, Eq. 11 and Eq. 14, the increment of plastic strain dp at time t can be obtained in terms of $\widehat{\mathbf{N}}_T$ and $\widehat{\mathbf{N}}_p$ as:

$$dp = \frac{\widehat{\mathbf{N}}_T : \widehat{\mathbf{N}}_p}{\sigma_T\left(\widehat{\mathbf{N}}_T\right)} \left|d\mathbf{E}^p\right| \tag{22}$$

The plastic flow direction can be defined as the direction of the plastic strain rate tensor, i.e.:

$$\widehat{\mathbf{N}}_p = \mathbf{E}_k^{p\bullet} / \left|\mathbf{E}_k^{p\bullet}\right| \tag{23}$$

Considering a sufficiently small strain increment, the plastic strain rate at time t can be evaluated as:

$$\mathbf{E}^{p\bullet} = \frac{\partial \mathbf{E}^p}{\partial t} \approx \frac{\mathbf{E}^{p(t)} - \mathbf{E}^{p(t-1)}}{\Delta t} = \frac{\Delta \mathbf{E}^{p(t)}}{\Delta t} \tag{24}$$

where $\mathbf{E}^p$ is the plastic strain tensor. Since the plastic deformation is isochoric in pressure-independent plasticity and, at large strains, the elastic part is small compared to the plastic one, the plastic strain tensor $\mathbf{E}^{p(t)}$ can be approximately reduced to the deviatoric part of the total strain tensor $\mathbf{E}^{(t)}$:

$$\mathbf{E}^p \approx \mathbf{E} - \frac{1}{3} tr\left(\mathbf{E}\right)\mathbf{I} \tag{25}$$

The total strain tensor is computed as the spatial logarithmic strain or Henky strain tensor:

$$\mathbf{E} = ln\mathbf{V} \tag{26}$$

where $\mathbf{V}$ is obtained by polar decomposition of the deformation gradient $\mathbf{F}$:

$$\mathbf{F} = \mathbf{V}\mathbf{R} \tag{27}$$

and $\mathbf{F}$ is computed from the displacement field $\mathbf{u}$:

$$\mathbf{F} = Grad\,\mathbf{u}\left(\mathbf{x}_0, t\right) + \mathbf{I} \tag{28}$$

The displacement $\mathbf{u}$ is measured by a full-field optical method during the experiment. The displacements are computed at coordinates $\mathbf{x}_0$ in the reference placement. This is what most commercial Digital Image Correlation (DIC, Sutton et al., 2009) software do, which is the reason why the reference placement has been considered here.

The strain tensor $\mathbf{E}^p$ however cannot be directly used to compute the stress. The deformation is defined in the global coordinate system while the plastic flow law and the yield function are written according to the material coordinate system aligned with the anisotropy axes, see Eq. 11.

Let us denote $\mathbf{R}|_{mat}$ the rotation tensor to rotate the global coordinate system into the material one in the reference placement. In the deformed

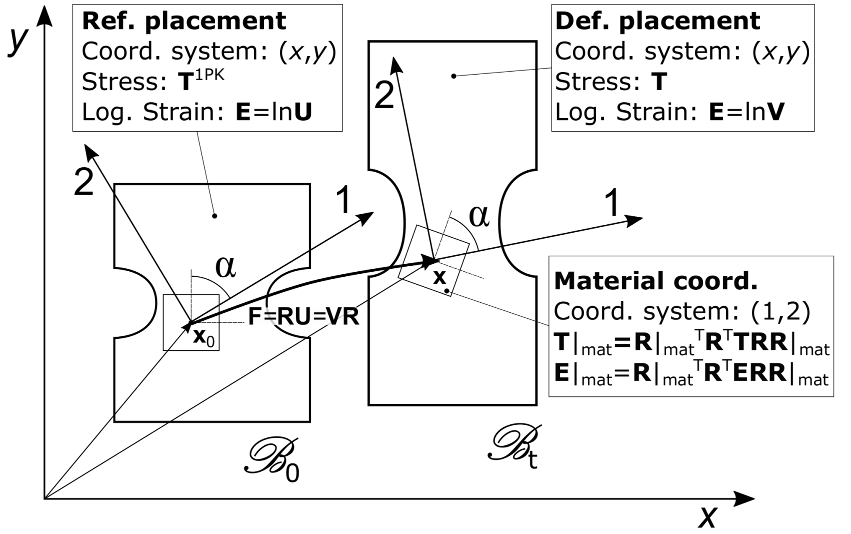

Figure 1: Finite deformation of the specimen, reference and current placement, rotation of the material axes and corresponding stress and strain tensors

configuration, the deformation tensor in the material coordinate system will be obtained by:

$$\mathbf{E}^p|_{mat} = \mathbf{R}|_{mat}^{T} \left(\mathbf{R}^T \, \mathbf{E}^p \, \mathbf{R} \, \right) \mathbf{R}|_{mat} \tag{29}$$

where $\mathbf{R}$ is the rotation tensor obtained in the polar decomposition of the deformation gradient tensor $\mathbf{F}$. The rotated strain tensor is used in Eqs. 23 and 24 to obtain the plastic flow versor $\widehat{\mathbf{N}}_p$. Then, Eqs. 14, 16 and 19 are applied to derive the Cauchy stress tensor $\mathbf{T}|_{mat}$, which is still in the material coordinate system. Finally, the Cauchy stress tensor is rotated back to global coordinate system:

$$\mathbf{T} = \mathbf{R}|_{mat} \left(\mathbf{R} \, \mathbf{T}|_{mat} \, \mathbf{R}^T \right) \mathbf{R}|_{mat}^{T} \tag{30}$$

The stress tensor, written in the global coordinate system, is used to obtain the 1st Piola-Kirchhoff tensor (Eq. 4), which will be used in the VFM formulation of Eqs. 7 and 8. Figure 1 shows a schematic of the specimen in the reference and deformed placements, and summarize the stress and strain tensors that have to be considered in the various cases.

2.3. Implementation of the Yld2000-2D model

In this section, the steps to implement the Yld2000-2D model in the stress computation routine are illustrated. This model will be used in Section 5 to identify the properties of a stainless steel sheet metal. This will allow to make a comparison with Hill48 in an actual case, showing some of the shortcomings of Hill48.

The equivalent stress for the Yld2000-2D criterion is:

$$\sigma_T\left(\mathbf{T}\right) = \left[\frac{1}{2}\left(\left|X_1' - X_2'\right|^a + \left|2X_2'' + X_1''\right|^a + \left|2X_1'' + X_2''\right|^a\right)\right]^{\frac{1}{a}} \tag{31}$$

where X_1', X_2' and X_1'', X_2'' are the principal values of the $\mathbf{X}'$ and $\mathbf{X}''$ tensors obtained from the Cauchy stress tensor $\mathbf{T}$ with the following transformation:

$$\begin{cases} \mathbf{X}' = \mathbf{L}'\mathbf{T} \\ \mathbf{X}'' = \mathbf{L}''\mathbf{T} \end{cases} \tag{32}$$

with $\mathbf{L}'$ and $\mathbf{L}''$:

$$\mathbf{L}' = \begin{bmatrix} \frac{2\alpha_1}{3} & -\frac{2\alpha_1}{3} & 0 \\ -\frac{2\alpha_2}{3} & \frac{2\alpha_2}{3} & 0 \\ 0 & 0 & \alpha_7 \end{bmatrix} \tag{33}$$

$$\mathbf{L}' = \begin{bmatrix} \frac{8\alpha_5-2\alpha_3-2\alpha_6+2\alpha_4}{9} & -\frac{4\alpha_6-4\alpha_4-4\alpha_5+\alpha_3}{9} & 0 \\ -\frac{4\alpha_3-4\alpha_5-4\alpha_4+\alpha_6}{9} & \frac{8\alpha_4-2\alpha_6-2\alpha_3+2\alpha_5}{9} & 0 \\ 0 & 0 & \alpha_8 \end{bmatrix} \tag{34}$$

and $\alpha_{1,\ldots,8}$ are the parameters that have to be identified. In order to compute the stress field, the same procedure as that described in Section 2.2 can be employed, using Eq. 31 instead of Eq. 11. With an associated flow rule, Eq. 13 is still valid:

$$\widehat{\mathbf{N}}_p = \frac{\mathrm{d}\,\Phi_p\left(\mathbf{T}\right)}{\mathrm{d}\,\mathbf{T}} \Bigg/ \left|\frac{\mathrm{d}\,\Phi_p\left(\mathbf{T}\right)}{\mathrm{d}\,\mathbf{T}}\right|$$

However, the computation of $\widehat{\mathbf{N}}_p$ is not straightforward because of the transformation. All the steps to compute the derivatives are detailed by Yoon et al. (2004). Afterwards, in order to compute the stress versor $\widehat{\mathbf{N}}_T$, Eq. 13 has to be inverted. In this case, this cannot be done directly as in Eq. 16. However it can be easily achieved numerically by interpolation.

Apart from these changes, the procedure for Yld2000-2D remains the same than the one described for Hill48.

2.4. Check of the plasticity occurrence

The procedure described above allows for computing the stress tensor if the considered strain increment is plastic. Therefore, at each step t, a check is performed to evaluate if the considered step is in the elastic or plastic domain

First, a trial stress ${\mathbf{T}_{trial}}^{(t)}$ is obtained assuming that the increment is purely elastic. Then, the yield criterion (Eq. 10) and the hardening law

(Eq. 20) are used to check if the element undergoes plastic deformation. Two cases are possible:

1. the element remains in the elastic domain

$$\sigma_T \left({\mathbf{T}_{trial}}^{(t)} \right) - \sigma_Y \left(p^{(t-1)} \right) < 0$$

$$\text{then} \begin{cases} \mathbf{T}^{(t)} = \mathbf{T}^{trial(t)} \\ p^{(t)} = p_k^{(t-1)} \end{cases}$$

2. the element is in the plastic domain

$$\sigma_T \left(\mathbf{T}^{trial(t)} \right) - \sigma_Y \left(p^{(t-1)} \right) > 0$$

$$\text{then} \begin{cases} \mathbf{T}^{(t)} \text{ computed from the routine of Sec. 2.2} \\ p_k^{(t)} = p^{(t-1)} + \Delta p^{(t)} \end{cases}$$

The current increment of plastic strain $\Delta p^{(t)}$ is computed using Eq. 22. The procedure is valid both for loading and unloading. If, within the same increment, some part is elastic and some plastic, as for instance when the first yielding occurs, the increment is subdivided in elastic and plastic parts.

2.5. Definition of the virtual fields

The optimal selection of virtual fields (VFs) for elasto-plasticity is still an open question. In elasticity, the most used system to generate optimised virtual fields was proposed byAvril et al. (2004): according to this method, special virtual fields are automatically generated in order to minimize the sensitivity to noise. Pierron et al. (2010) also applied a similar approach in plasticity but with a relative success only. Indeed, in plasticity, the level of deformation is usually much larger than in elasticity and the noise-to-signal ratio is small. This means that noise sensitivity is most relevant optimisation criterion to define virtual fields and other strategies have to be considered.

Here, the virtual fields have been selected empirically based on previous experience from the authors. The problem of automatic definition of optimized virtual fields is still an outstanding problem in the Virtual Fields Method, however, progress on this is expected soon and will be released in a future publication. This is of particular importance for anisotropic plasticity where the relative contribution of the different stress components to the cost function is of primary interest. Here, the following virtual fields were defined, as a first attempt to include all stress components in the cost function:

$$\delta\mathbf{v}^{(1)} = \begin{cases} \delta v_x = 0 \\ \delta v_y = \dfrac{y}{H} \end{cases}$$

$$\delta\mathbf{v}^{(2)} = \begin{cases} \delta v_x = \dfrac{x}{W}\dfrac{(|y| - H)}{H} \\ \delta v_y = 0 \end{cases} \tag{35}$$

$$\delta\mathbf{v}^{(3)} = \begin{cases} \delta v_x = \delta v_y = \frac{1}{\pi}\sin\left(\pi\frac{x}{W}\right)\cos\left(\pi\frac{y}{2H}\right) \end{cases}$$

H and W are the height and the width of the specimen area where the VFM is defined. When $y = \pm H$, $\delta v_x = 0$ and δv_y is constant ($\delta\mathbf{v}^{(1)}$) or zero ($\delta\mathbf{v}^{(2)}$ and $\delta\mathbf{v}^{(3)}$). Such condition allows simplifying the second integral of Eq. 7 so that only the resultant of the forces in the y-direction, i.e. the load measured during the test by the load cell, is used to compute the external virtual work.

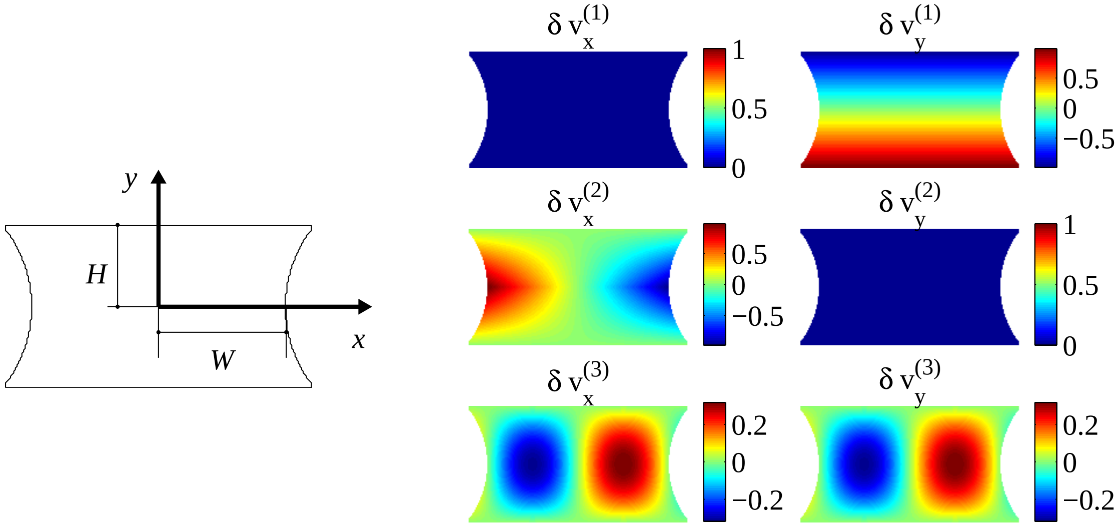

Figure 2: Schematic of the origin of axes and plot of $\delta\mathbf{v}$ for the three considered VFs

This operation is typical in VFM practise and will not be commented further, more details are given by Pierron and Grédiac (2012). The origin of axes x and y is placed at the centre of the specimen, as illustrated in Figure 2. The same figure also plots the components ot the used VFs.

The gradient $\delta\mathbf{F}^{\bullet}$ of the virtual displacement writes:

$$\delta \mathbf{F}^{\bullet\,(1)} = \begin{bmatrix} 0 & 0 \\ 0 & \dfrac{1}{H} \end{bmatrix}$$

$$\delta \mathbf{F}^{\bullet\,(2)} = \begin{bmatrix} \dfrac{(|y| - H)}{WH} & \operatorname{sgn}(y)\,\dfrac{x}{WH} \\ 0 & 0 \end{bmatrix} \tag{36}$$

$$\delta \mathbf{F}^{\bullet\,(3)} = \begin{bmatrix} \frac{1}{W}\cos\left(\pi \frac{x}{W}\right)\cos\left(\pi \frac{y}{2H}\right) & -\frac{1}{2H}\sin\left(\pi \frac{x}{W}\right)\sin\left(\pi \frac{y}{2H}\right) \\ \frac{1}{W}\cos\left(\pi \frac{x}{W}\right)\cos\left(\pi \frac{y}{2H}\right) & -\frac{1}{2H}\sin\left(\pi \frac{x}{W}\right)\sin\left(\pi \frac{y}{2H}\right) \end{bmatrix}$$

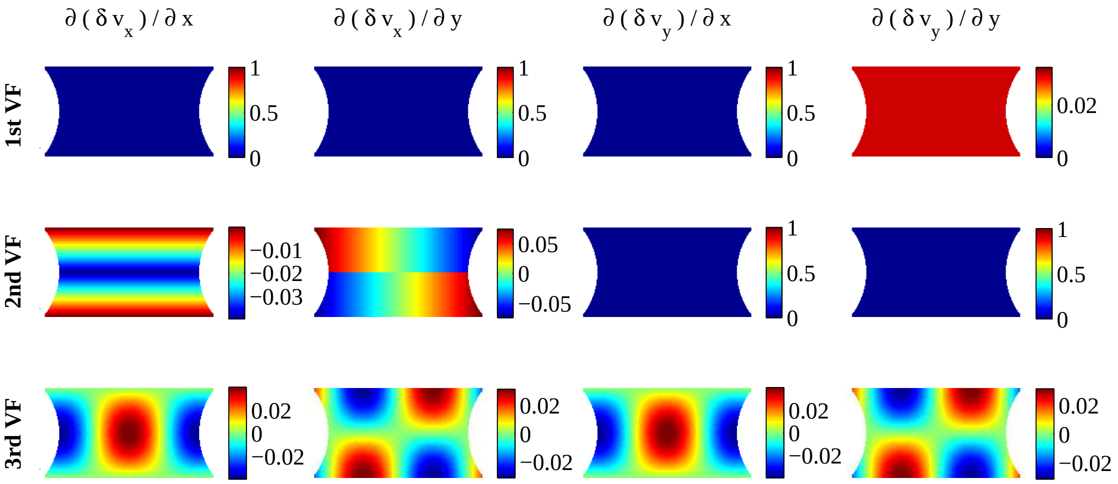

Figure 3: Plot of the components of $\delta \mathbf{F}^{\bullet}$ for the three considered VFs

In order to compute the internal virtual work (first integral of Eq. 7), each component of Piola-Kirchhoff stress tensor $\mathbf{T}^{1PK}$ is multiplied by the corresponding component of $\delta \mathbf{F}^{\bullet}$. Using the 1st VF, only T_{yy}^{1PK}, that is the stress component in the loading direction, is considered in the internal virtual work. The 2nd VF, instead, involves T_{xx}^{1PK} and T_{xy}^{1PK}. The 3rd VF, finally, has all non-zero components, therefore it activates all the four components of $\mathbf{T}^{1PK}$.

A graphical representation of the three VFs is provided in Figure 3, the contour maps shows that the average value is similar for the different VFs, so that, when they are used together in Eq. 8, their relative weight is comparable.

3. Numerical validation

The numerical validation was performed using FE simulations that reproduce a tensile test on notched specimens, using the Hill48 criterion. Figure 4a illustrates the geometry of the specimen, which is the same as that used in the experiments. The notched shape is often used because it is able to produce an heterogeneous strain field, is easy to machine, and, in plasticity, allows to have a large zone of the specimen under plastic deformation. This is particularly valuable looking at large strains, while for instance $\Sigma-$shaped specimens, like the ones proposed by Kim et al. (2014), localize the strain in a small area and leaves the majority of the specimen at low deformations. However, the design of an optimized specimen is still an open problem. Recent advances in test specimen design for orthotropic elasticity have been published (Gu and Pierron, 2016) based on a simulator which reproduces the whole identification process, also taking into account the systematic errors caused by the DIC measurements. Extension of this to elasto-plasticity is on the way, although this will be greatly computationally expensive as many identification problems need to be solved in the process. In any case, this is beyond the scope of the present paper.

In the future optimization methods could be adopted to find out the best geometry, as done for instance by Wang et al. (2016) for polymeric foams or by Rossi and Pierron (2012b) for orthotropic composite materials.

The element orientation can be varied with respect to the loading direction, in order to reproduce specimens cut in different directions. As a convention, angle α measures the rotation between the rolling and the loading direction. The global coordinate system is denoted $\{x, y\}$, where y is the loading direction, while the local coordinate system is denoted $\{1, 2\}$, where 1 represents the rolling direction.

The FE model illustrated in Figure 4b was built up with ABAQUS standard, using CPS4 elements (four nodes, bilinear shape functions, full integration) and large displacement formulation. A total displacment of 30 mm (10% of the specimen's length) was applied to one end of the specimen. Figure 4b shows the used mesh and a contour plot of the equivalent plastic strain at the last increment of the test, which is around 0.5. The contour map indicates that the deformation field, and accordingly the stress field, is heterogeneous thanks to the round notches at the sides of the specimen.

The nature of the generated stress field can be better depicted in the graph of Figure 5, which plots a 2D view of the yield surface. In this type of graphs, used for instance by Barlat et al. (2003), the horizontal and vertical axes represent the σ_{11} and σ_{22} stress components, normalized according to the equivalent stress. The 3rd axis, perpendicular to the figure plane, represents the normalized shear stress σ_{12}. The anisotropic yield surface can be therefore represented as contour lines, where the external line represent the

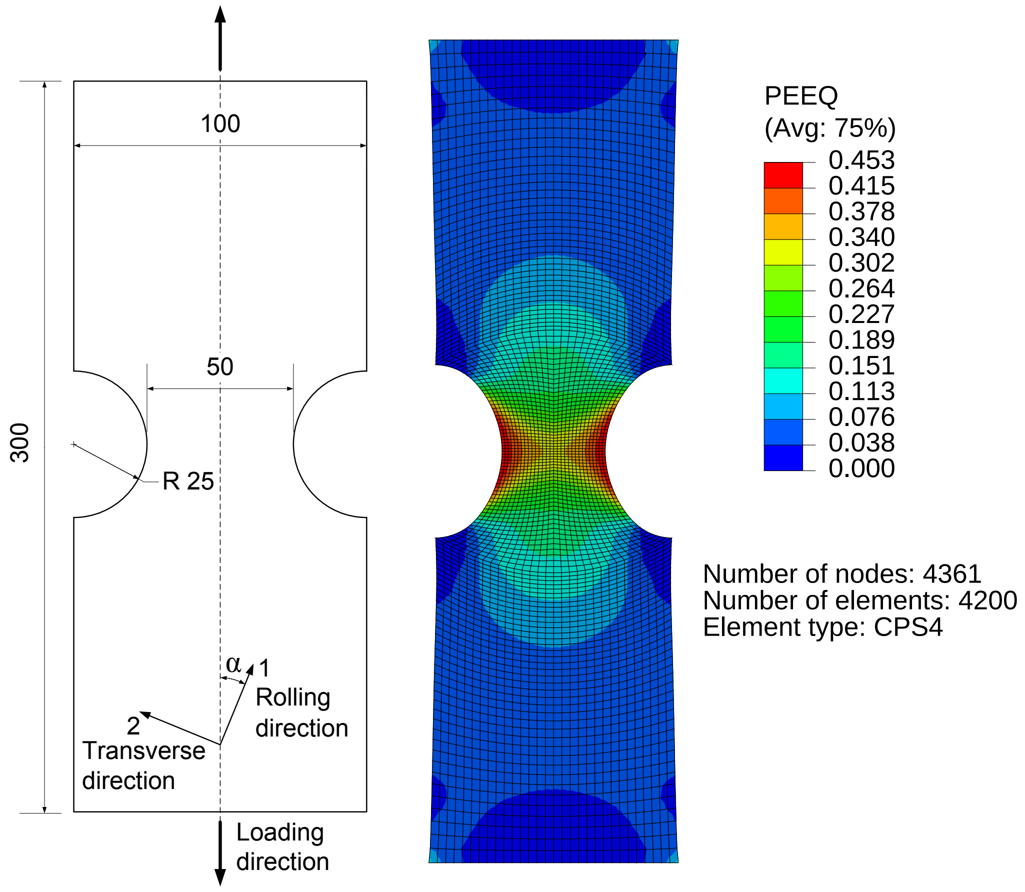

(a) Geometry (b) FEM

Figure 4: Specimen geometry (units: mm) and corresponding FE model. The equivalent plastic strain map is shown for an end's displacement of 30 mm ($\alpha = 0°$)

yield surface when the shear stress $\sigma_{12} = 0$ and the origin is the condition of pure shear.

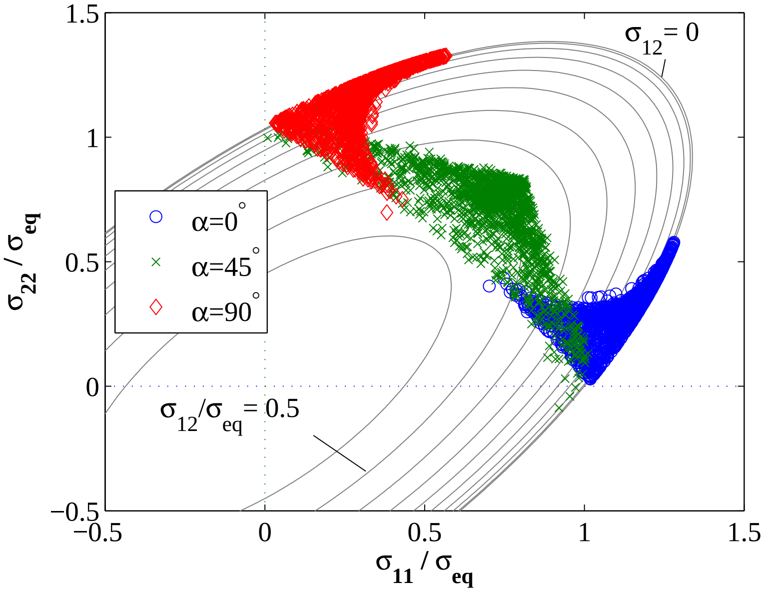

Figure 5: Distribution of the stress

In this chart, each point represents a different state of stress. Since the stress is normalized, all points of all time steps can be introduced in the same graph. A practical recommendation of the VFM is that the specimen should produce a sufficiently heterogeneous state of stress, so that different stress conditions can be evaluated at the same time. With the adopted configuration, using a single specimen, only a small part of the yield surface can be covered, as illustrated in Figure 5. For instance, using a specimen with $\alpha = 0^\circ$, only the zone close to uniaxial tensile tension in the 1st direction is covered. Also, even when using notched specimens at three different orientations, the pure shear and the biaxial conditions cannot be reached.

As a first numerical check, the VFM was applied to the strain maps generated with the FEM computations without any noise. In order to check the stress reconstruction algorithm described in Section 2.2, Figure 6 shows a comparison between the Cauchy stress tensor computed by FEM and the one obtained from the displacement field using the proposed method. A good agreement is found.

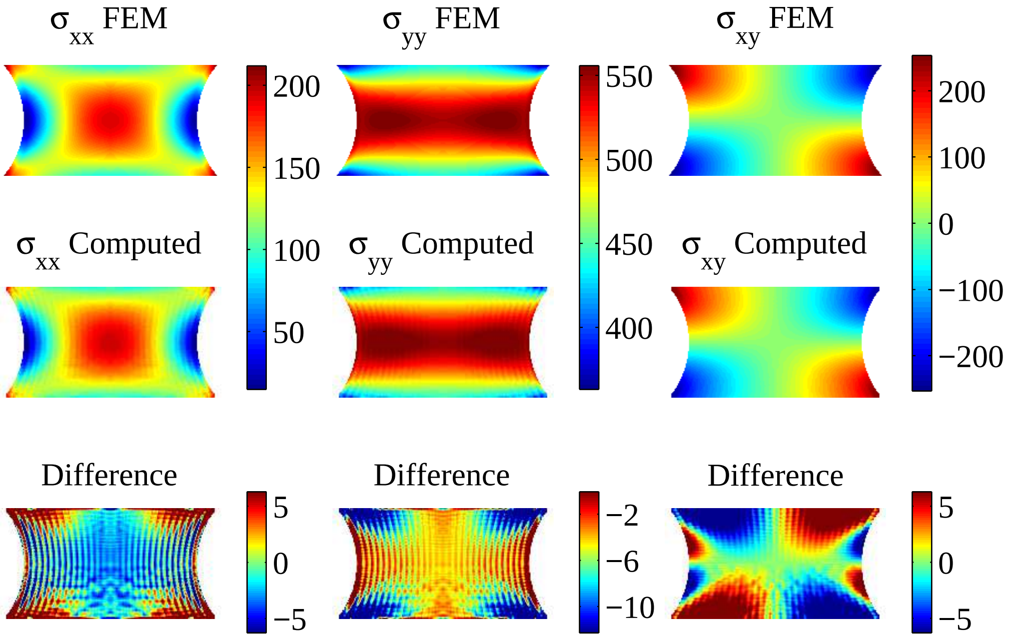

Figure 6: Comparison between the FEM and computed stress components using the reconstruction routine

The results of the identification with the VFM are summarized in Table 1. The combination of 3 VFs always improves the identification. Using a single specimen at 0°, R_{90} cannot be identified and conversely for R_0 with a specimen at 90°.

The specimen cut at 45° however allows to correctly identify all parameters, with an error lower than 1%, when the three VFs are used. Similar results are obtained introducing both 0° and 90° specimens in the cost function. These results can be explained looking at the graph of Figure 5, the 45° specimen covers a larger part of the yield surface and allows looking at both anisotropy directions. The same result can be obtained combining the 0° and 90° specimen.

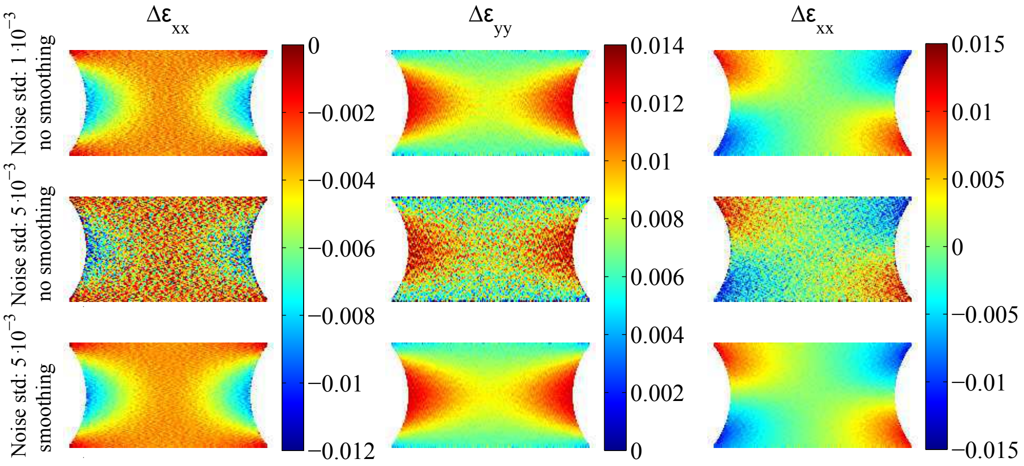

Figure 7: Strain increment fields with noise, without and with temporal smoothing

A second validation was conducted to evaluate the effect of noise. Dealing with large deformation, noise has a minor impact on identification, however, in order to define the direction of the plastic flow, the strain increment $\Delta\mathbf{E}$ is used in Eq. 24. This value can be small enough so that noise plays a role. Two levels of noise were considered with a standard deviation of 10^{-3} and $5 \cdot 10^{-3}$, respectively. The first represents a rather large strain uncertainty

Specimen configurations	Virtual Fields	identified parameters					
		K	ε_0	N	R_0	R_{45}	R_{90}
	Reference	1000	0.02	0.5	1.8	1.1	2.5
0°	$VF1$	1208.5	0.0171	0.4799	0.58	0.33	0.47
	Error	-20.85%	14.52%	4.02%	67.56%	70.04%	81.32%
	$VF1 + VF2$	1010.2	0.0169	0.4812	1.93	1.05	1.20
	Error	-1.02%	15.46%	3.77%	-7.44%	4.67%	52.00%
	$VF1 + VF2 + VF3$	1017.1	0.0176	0.4871	1.79	1.17	1.47
	Error	-1.71%	12.19%	2.58%	0.65%	-6.72%	41.17%
90°	$VF1$	1048.8	0.0188	0.5049	2.17	1.61	2.38
	Error	-4.88%	6.03%	-0.98%	-20.49%	-46.55%	4.98%
	$VF1 + VF2$	975.6	0.0201	0.5030	1.74	1.01	2.62
	Error	2.44%	-0.48%	-0.61%	3.49%	8.37%	-4.61%
	$VF1 + VF2 + VF3$	702.0	0.0207	0.4714	0.62	1.07	2.58
	Error	29.80%	-3.38%	5.72%	65.63%	2.94%	-3.14%
45°	$VF1$	906.0	0.0198	0.4982	2.32	1.21	3.00
	Error	9.40%	0.78%	0.36%	-29.14%	-10.30%	-20.00%
	$VF1 + VF2$	1014.7	0.0198	0.5035	1.57	1.12	2.59
	Error	-1.47%	1.10%	-0.70%	12.96%	-1.97%	-3.58%
	$VF1 + VF2 + VF3$	994.5	0.0197	0.5016	1.80	1.09	2.50
	Error	0.55%	1.49%	-0.32%	0.21%	1.00%	-0.15
0° + 90°	$VF1$	992.9	0.0189	0.4987	1.79	1.47	2.47
	Error	0.71%	5.66%	0.25%	0.79%	-33.74%	1.30%
	$VF1 + VF2$	995.7	0.0200	0.5047	1.84	1.03	2.56
	Error	0.43%	0.01%	-0.94%	-2.23%	6.59%	-2.51%
	$VF1 + VF2 + VF3$	1005.3	0.0196	0.5029	1.77	1.11	2.45
	Error	-0.53%	1.79%	-0.59%	1.41%	-0.84%	2.01%

Table 1: Results of the numerical validation, different combination of VFs and specimen orientations are considered

for DIC measurements (Sutton et al., 2009), the second a severe (unrealistic) noise condition. Noise was directly applied as a random number to the strain field. For the higher noise condition, temporal smoothing (Le Louëdec et al., 2013) was introduced to reduce the noise effect, as illustrated in Figure 14. Temporal smoothing was performed by computing the strain rate at time t using more time steps and performing a polynomial fitting. This can be efficiently implemented using a convolution method as the one provided by Savitzky and Golay (1964).

The strain rate of Eq. 24 can be rewritten as:

$$\mathbf{E}^{p\bullet} = \frac{\partial \mathbf{E}^p}{\partial t} \approx \frac{\displaystyle\sum_{j=-m}^{m} h_j \mathbf{E}^{p(t+m)}}{\Delta t} \tag{37}$$

thus, the strain rate at the time t is computed using $2m+1$ steps. A procedure to compute the convolution weights h_j is given by Gorry (1990), the method allows considering also the end points of the data set. In the present case, the smoothing was performed using 7 points ($m = 3$).

Table 2 shows the parameters identified for the different cases. With the low noise level, all parameters are identified with a good confidence, even if no smoothing is applied. With the high noise level, the identification is not correct, with errors over 10% for most of the identified parameters. As expected, looking at the anisotropy parameter R, using the 45° specimen a poor identification is obtained for R_0 and R_{90}; combining the 0° and 90° specimens, a larger error is obtained for R_{45}. With temporal smoothing, a correct identification is obtained for all parameters except ε_0. However, this parameter, used in Eq. 20, has a marginal impact in the definition of

Specimen configurations	Noise standard deviation	Identified Parameters					
		K	ε_0	N	R_0	R_{45}	R_{90}
	Reference	1000	0.02	0.5	1.8	1.1	2.5
45°	$1 \cdot 10^{-3}$	983.7	0.0188	0.4966	1.88	1.08	2.50
	Error	1.63%	5.92%	0.67%	-4.69%	1.80%	0.16%
	$5 \cdot 10^{-3}$	807.8	0.0022	0.4065	3.00	1.00	2.96
	Error	19.22%	89.13%	18.70%	-66.67%	8.72%	-18.48%
	$5 \cdot 10^{-3}$ smoothed	974.9	0.0277	0.5018	1.80	1.09	2.62
	Error	2.51%	-38.50%	-0.37%	-0.09%	1.21%	-4.76%
$0° + 90°$	$1 \cdot 10^{-3}$	999.6	0.0184	0.4951	1.78	1.12	2.45
	Error	0.04%	8.04%	0.98%	1.15%	-1.64%	1.81%
	$5 \cdot 10^{-3}$	918.0	0.0001	0.3714	1.80	1.31	2.48
	Error	8.20%	99.50%	25.72%	-0.18%	-19.20%	0.68%
	$5 \cdot 10^{-3}$ smoothed	1002.4	0.0295	0.5079	1.78	1.13	2.46
	Error	-0.24%	-47.68%	-1.59%	1.09%	-2.73%	1.73%

Table 2: Influence of noise on VFM identification

the hardening law (Rossi and Pierron, 2012a). Therefore its variation does not introduce significant modification in the identified true stress-true strain curve.

The main outcomes of the numerical validation can be summarized as follow:

- the effectiveness of the VFM depends on the heterogeneity of the stress field. The spread of stress distribution can be visualized conveniently in a normalized stress plane (Figure 5);

- the adopted notched specimens generate a state of stress that spans

Specimen configuration	Virtual Fields	Iter.	Ψ eval.	CPU time [s]	Ψ av. time [s]
0°	$VF1$	74	604	1335	2.2
	$VF1 + VF2$	74	606	1333	2.2
	$VF1 + VF2 + VF3$	76	602	1328	2.2
$0° + 90°$	$VF1$	55	538	2367	4.4
	$VF1 + VF2$	55	537	2362	4.4
	$VF1 + VF2 + VF3$	56	519	2284	4.4

Table 3: CPU time used to perform the identification

only a small part of the yield surface. However, for the Hill48 criterion, good identification can be obtained using a 45° specimen or the combination of 90° and 0°;

- the combination of three virtual fields allows reducing the identification error;
- strain noise does not represent a major problem. In case of severe noise, temporal smoothing applied to the strain field significantly increases the quality of the identification.

3.1. Computational time

In the eventuality of using an inverse identification method at the industrial level, the computational time becomes an important aspect that should be taken into consideration. One advantage of the VFM is that the identification routine is rather fast compared to, for instance, finite element updating, where an FE model has to be run for each iteration.

Table 3 shows the time required to perform the identification. The analysis was performed with a standard computer (Intel® Core$^{\text{TM}}$ 2 CPU 6700 @ 2.66GHz 2.66GHz, RAM: 4.00 GB) using non-optimized Matlab routines.

The time required for a single iteration is about 2.2 s when a single test is considered. This is more or less constant regardless of the number of virtual fields used in the cost function. The time for a cost function evaluation is however doubled when a second test is introduced because of the stress reconstruction. On the other hand, when two tests are used, the number of iterations required to identify the parameters is reduced from $74-76$ to $55-56$. Therefore the overall CPU time needed to perform the identification is less than double compared to the identification with a single test.

This computational time could be definitely reduced using faster programming languages and higher CPU speed, showing the potentiality of this method to be used in industrial applications, where time is an important added value.

4. Experiments

The experiments were conducted on notched specimens with the same geometry used in the numerical validation, and illustrated in Figure 4a. The specimens were cut from a blank sheet of stainless steel, 0.75 mm thick. Three different cutting directions were used: 0°, 45° and 90°. The yield stress and the Lankford parameter measured in the three directions by standard uniaxal

Dir.	Thick.	$R_p0.2$	R_m	$A80$	A_g	R				
						3%	5%	10%	15%	20%
	mm	MPa	MPa	%	%					
0°	0.75	128	296	45	25	1.8	1.9	1.9	1.9	1.9
45°	0.75	138	305	43	24	1.5	1.5	1.5	1.6	1.6
90°	0.75	132	294	44	25	2.1	2.1	2.2	2.2	2.3

Table 4: Results of uniaxial test according to EN 10002-1 for three directions . R is evaluated at different levels of engineering strain

tests, according to the EN 10002-1 standard[2], are listed in Table 4.

The full-field displacement field was obtained by stereo Digital Image Correlation (DIC), using the commercial software VIC-3D. We used black and white sprays to create the speckle pattern onto the specimen surface (white background and black speckles). The thickness of the paint was kept thin so that it was able to undergo large deformation without flaking. An example of the speckle pattern obtained during the test is illustrated in Figure 9. It is able to follow the deformation of the specimen up to the final fracture.

The experimental set-up is illustrated in Figure 8. An INSTRON-880 tensile machine with hydraulic grips was used to perform the tests. The cameras are two JAI Pulnix TM-4000CL. Table 5 summarizes the information about the sensor, the camera noise, the DIC settings and the displacement and strain resolution.

---

[2] $R_p0.2$ = 0.2 % offset yield strength; R_m = tensile strength at maximum force; $A80$ = percentage elongation after fracture; A_g = Percentage elongation at maximum force.

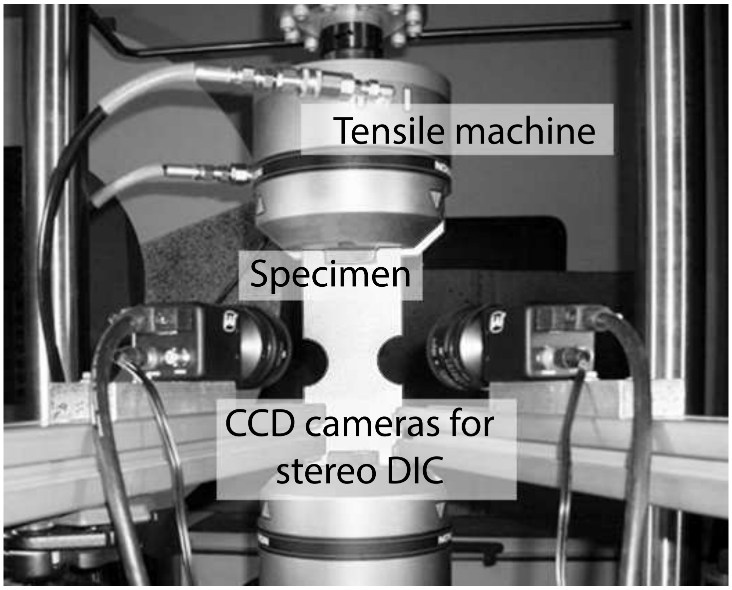

Figure 8: Experimental set-up

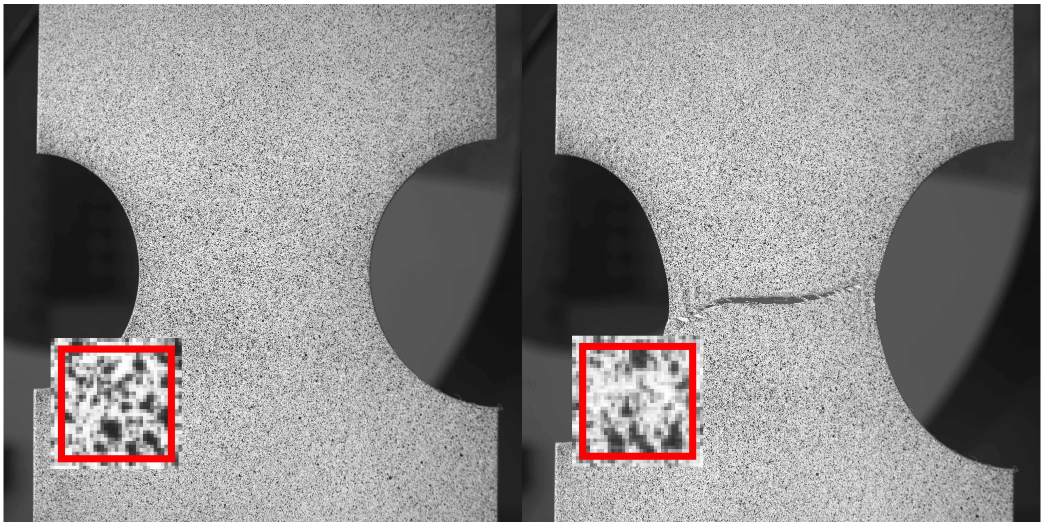

Figure 9: Example of the speckle pattern used during the test in the undeformed and deformed configuration.

Technique used	Stereo digital image correlation
Sensor and digitization	2048 × 2048, 10-bit
Camera noise (% of range)	0.6 %
Pixel to mm conversion	1 pixel = 0.055 mm
ROI (mm)	100 mm × 80 mm
Subset, step	27, 5
Interpolation, shape functions,	bilinear, affine
Correlation criterion	ZNSSD
Pre-smoothing	Gaussian 5
Displacement resolution	0.01 pixels, 0.55 μm
Strain derivation	2nd order polynomial fitting
Strain window	5 × 5
Strain resolution	$2.5 \cdot 10^{-4}$

Table 5: Sensor characteristics, DIC settings, displacement and strain resolution.

The correlation algorithm was run using a subset window of 27 pixels and a step of 5 pixels between two measurement points. The incremental correlation options was used, i.e. each image is correlated with the previous one and the measured incremental displacement is added to the one measured in the previous step. Figure 10 shows an example of displacement fields obtained from the experiments, the red box highlights the zone of the specimen used subsequently for the VFM. In this zone, with the adopted settings, 101×216 measurement points were obtained for each step.

The VFM was restricted to this smaller zone for two reasons: first, it remains planar up to large strains whereas the external parts of the specimen tend to wrinkle as the deformation increases; secondly, the plastic flow localizes within this zone while the external parts mainly remains in the elastic regime. In the future, however, the geometry and the experimental set-up should be modified to better exploit the spatial resolution of the stereo-DIC measurement.

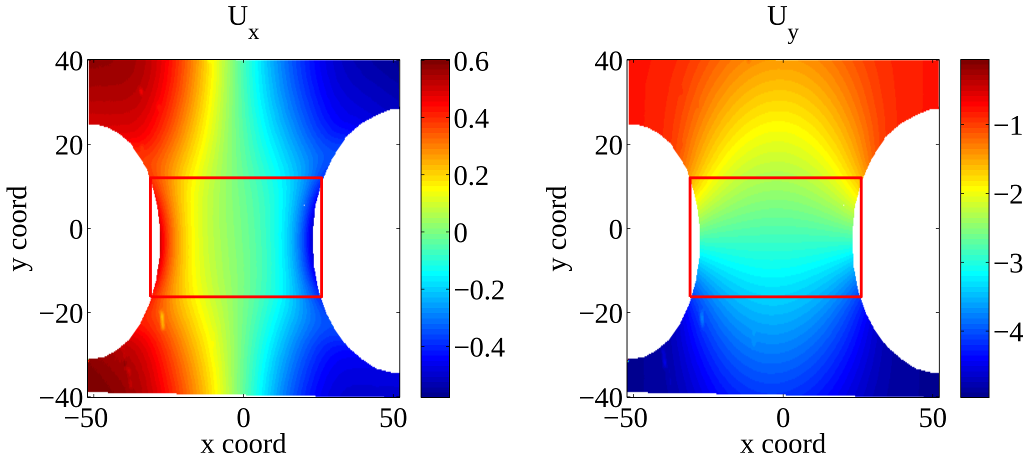

Figure 10: Displacement field measured by stereo DIC, the zone used to perform the identification is highlighted by the red box

Stereo DIC allows recording out-of-plane movements, which can be caused by misalignments of the camera with respect to the specimen surface or by instabilities (buckling, wrinkling, etc.) of the sheet metal during deformation. In this case, plastic instabilities occurs in all specimens at the final stage of the test. Figure 11 shows the onset of instability in terms of out of plane displacement. Nonetheless, 48 time steps were recoreded before the onset of instability and used to perform the VFM identification. At the final available step, the maximum engineering strain was around 20%, which is already in the large plasticity region. In the future, in order to investigate larger strains,

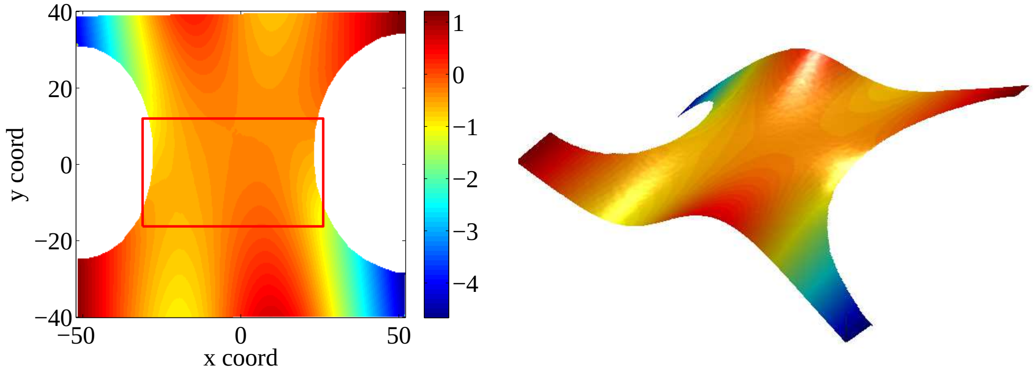

Figure 11: Out of plane movements measured after the onset of plastic instability

the shape of the specimen should be optimized to avoid, or postpone, the instability.

The cameras were synchronized with the load cell so that, for each image, the system records the corresponding tensile force. The measured force versus displacement curves are plotted in Figure 12. The variation between the tests is due to the anisotropic behaviour of the material.

5. Results and discussion

In the following section, the parameter identification performed with the VFM from the experimental data is discussed.

5.1. Application of the Hill48 criterion

First, the VFM was used with the experimental data in order to identify the parameters of the Hill48 model. The logarithmic strain $\mathbf{E}$ (Eq. 26) at each step was computed from the measured displacement field. Spatial smoothing was used before differentiation by fitting the best second order polynomial

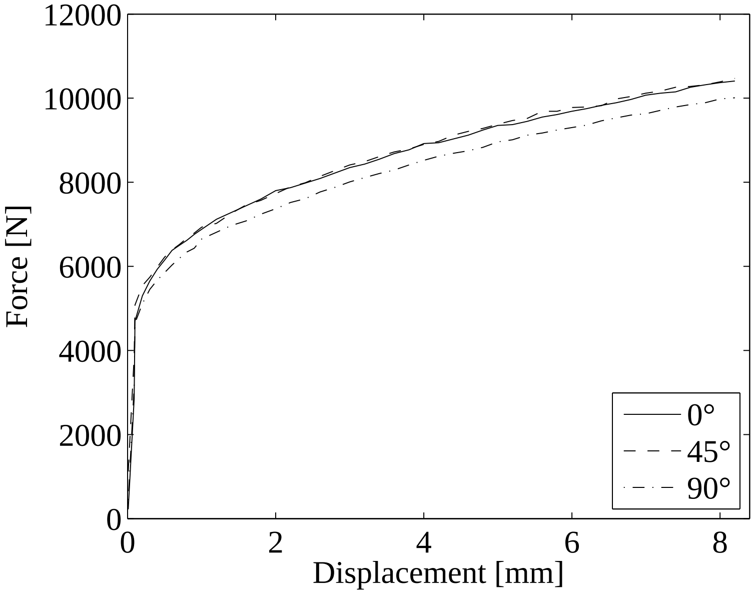

Figure 12: Force measured for the three tests

to a 5 × 5 data points window. Strain components were obtained from the polynomial coefficients. A simple noise analysis performed on still images of the same specimen provided a standard deviation of strain of around $2.5{\cdot}10^{-4}$. This value is comparable with other published data (Badaloni et al., 2015).

Figure 13 shows a typical strain map obtained during the tests, for the three strain components. Because of the large deformation and the favourable noise-to-signal ratio, the total strain fields were only marginally affected by noise.

As mentioned in Section 3, the effect of noise is visible on the strain increments $\Delta\mathbf{E}$. In this case, temporal smoothing was performed over 5 time steps to reduce noise ($m = 2$). Figure 14 show the strain increment fields before and after temporal smoothing.

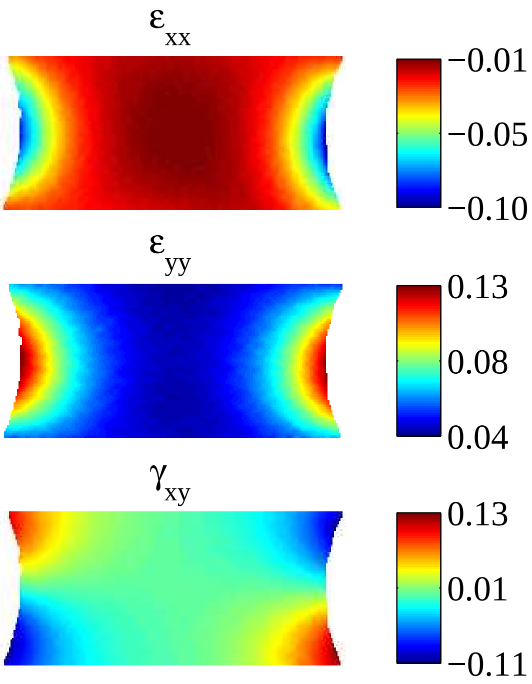

Figure 13: Example of strain fields obtained from the stereo DIC measurement (Force: 9.7 kN, direction: 90°)

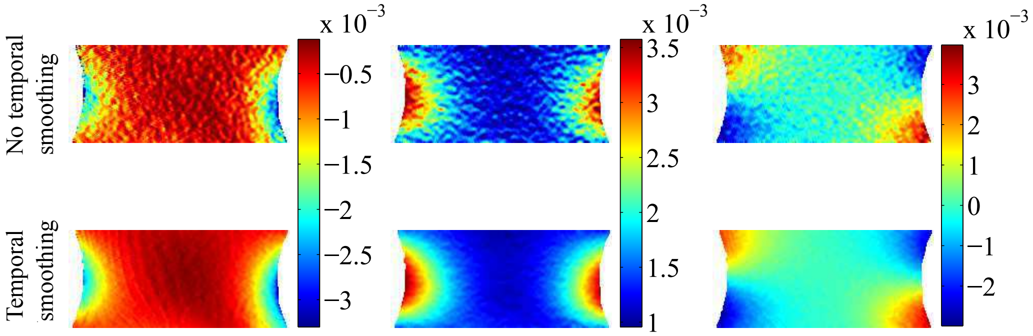

Figure 14: Experimental strain increments, with and without temporal smoothing (Force: 9.7 kN, direction: 90°)

Specimen	Identified parameters						Cost function
configuration	K	ε_0	N	R_0	R_{45}	R_{90}	
0°	1183	0.035	0.64	1.76	0.94	0.3	192
90°	439	0.012	0.43	0.46	0.77	2.20	207
45°	888	0.012	0.43	1.10	1.35	0.78	115
0° + 90°	665	0.010	0.41	1.95	0.78	1.82	423
0° + 45° + 90°	735	0.010	0.41	1.21	1.32	1.12	576
Reference	-	-	-	1.88	1.56	2.18	

Table 6: Experimental results

Table 6 reports the identified parameters and the reference R values obtained from the standard uniaxial tests, see Table 4. In this case, the hardening parameters, K, ε_0 and N, cannot be directly compared with reference experimental values. However, a comparison with the experiments can be performed in terms of tensile force. The load L_i, measured experimentally at each step i, can be indeed compared with the force computed using the identified parameters and the measured strain field. Following the definition of VF1 (Eq. 35):

$$\int_{\partial \mathscr{B}_0} \left(\mathbf{T}^{1PK}\mathbf{n}_0\right) \cdot \delta\mathbf{v}^{(1)}\, da_0 = 2L_i \tag{38}$$

and, from Eq. 3:

$$L_i = \frac{1}{2}\int_{\mathscr{B}_0} \mathbf{T}_i^{1PK} \cdot \delta\mathbf{F}^{\bullet\,(1)}\ dv_0 \tag{39}$$

where $\mathbf{T}_i^{1PK}\left(\bar{\boldsymbol{\xi}}, \boldsymbol{u}|_{0\to t}\right)$ is obtained from the measured displacement field using the identified constitutive parameters $\bar{\boldsymbol{\xi}}$. Figure 15 shows the comparison between the measured force and the force reconstructed from the strain and the material model, for all time steps (horizontal axis). As expected, using a single test at 0° or 90°, the parameters of the corresponding directions are correctly identified while a large error is encountered for the other directions. Using the specimen at 45°, the error diminished but the load in the 0° direction is still not reproduced correctly. Using $0° + 90°$, the load at 45° is not reproduced correctly. When all tests in the three directions are used in the cost function, the force is correctly reproduced in all cases.

The identification of R in the different directions is more critical: looking at Table 6, using a single direction, the R values are similar to the experimental reference only for the corresponding directions. Using $0° + 90°$, R_{45} is not well identified. When all specimens are used, all values of R are rather different from the reference.

The reason for this is that, in this case, the Hill48 model is not able to reproduce the behaviour of the material. When the cost function is constrained with all tests, the VFM identifies the best set of parameters for the Hill48 model, which is however not able to describe the material behaviour.

The cost function (Ψ), obtained at the end of the minimization, can be considered an indicator of the quality of the identification (Rossi et al., 2014). In this case, the cost function is larger when all three tests are considered. This suggests that, when more tests are used at the same time, the minimization algorithm is not able to reduce the error beyond a certain limit.

Figure 16 illustrates the stress states mapped onto the yield surface for the experiments. The map is very similar to the one obtained for the numerical case (Figure 5), and shows the zone of the yield function covered by the

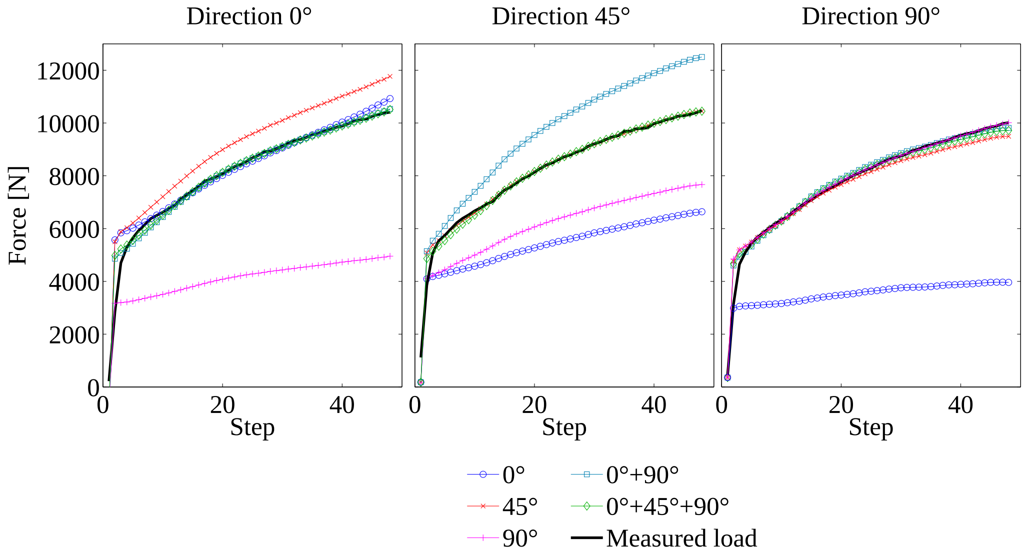

Figure 15: Comparison between the experimental load and the one computed using the strain field and the identified parameters

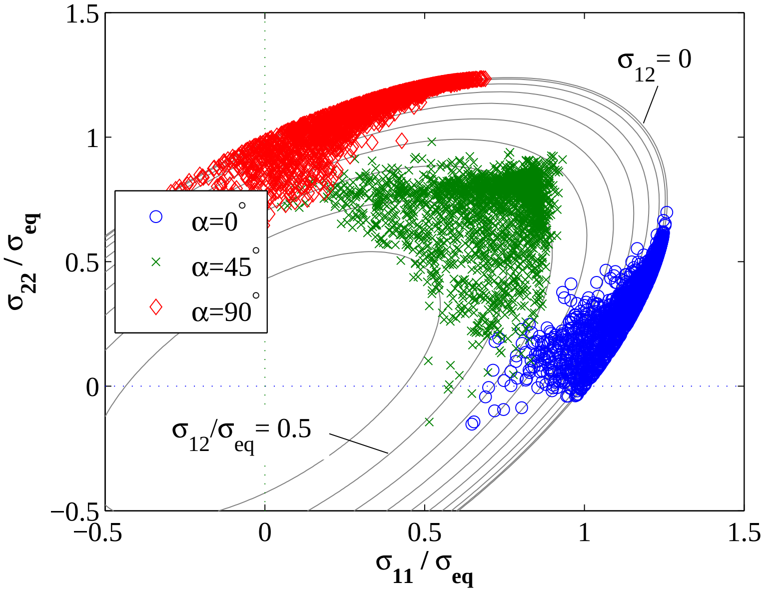

Figure 16: Distribution of the stress states in the experiments

performed experiments.

5.2. Application of the Yld2000-2D criterion

The Hill48 criterion is not able to reproduce the behaviour of the tested material. In order to support this statement, the same VFM approach was employed to identify the parameters of the Yld2000-2D model (Barlat et al., 2003).

In this case 11 parameters have to be identified from the minimization algorithm, 3 for the hardening law and 8 for the yield function. This model is more versatile than Hill48, where only 3 parameters are used to describe the anisotropy.

The identification was conducted using the three tests (0° + 45° + 90°) and the same three VFs used for Hill48. As first guess, the Yld2000-2D parameters are set equal to 1 ($\alpha_{1,\ldots,8} = 1$), while the hardening parameters (K , ε_0, N) are set equal to the ones identified with the Hill48 criterion.

In spite of the rather large number of parameters, the minimization algorithm was able to converge to a set of parameters as listed in Table 7. In order to check the stability of the identified parameters, different initial conditions were tested. Two sets of parameters were generated randomly and used as first guess in the minimization algorithm. The results obtained with the different sets of initial guess are compared in Table 8. A slight variation is observed in the hardening parameters, while the anisotropic parameters α_i are not sensitive to the initial guess. Thus, the identification procedure can be considered sufficiently stable.

Figure 17 shows the distribution of the stress states in the identified yield function. Figure 18 shows the comparison of the two models in terms of

Hardening			Yld2000-2D parameters							
K	ε_0	N	α_1	α_2	α_3	α_4	α_5	α_6	α_7	α_8
852	0.01	0.41	1.11	1.35	1.21	1.11	1.07	0.96	1.21	1.15

Table 7: Parameters identified from the experimental tests using Yld2000-2D

	Initial guess										
	K	ε_0	N	α_1	α_2	α_3	α_4	α_5	α_6	α_7	α_8
set 1	735	0.01	0.41	1.00	1.00	1.00	1.00	1.00	1.00	1.00	1.00
set 2	1240	0.015	0.3	1.55	1.60	1.48	1.83	1.23	1.01	1.94	0.68
set 3	520	0.05	0.7	1.54	1.16	1.12	0.72	1.31	0.79	1.62	1.57
	Identified parameters after minimization										
	K	ε_0	N	α_1	α_2	α_3	α_4	α_5	α_6	α_7	α_8
set 1	852	0.01	0.41	1.11	1.35	1.21	1.11	1.07	0.96	1.21	1.15
set 2	910	0.01	0.42	1.11	1.34	1.20	1.10	1.07	0.95	1.20	1.15
set 3	805	0.01	0.39	1.10	1.36	1.22	1.10	1.07	0.95	1.21	1.14

Table 8: Influence of initial guess in the minimization process, set 2 and set 3 were obtained using random numbers.

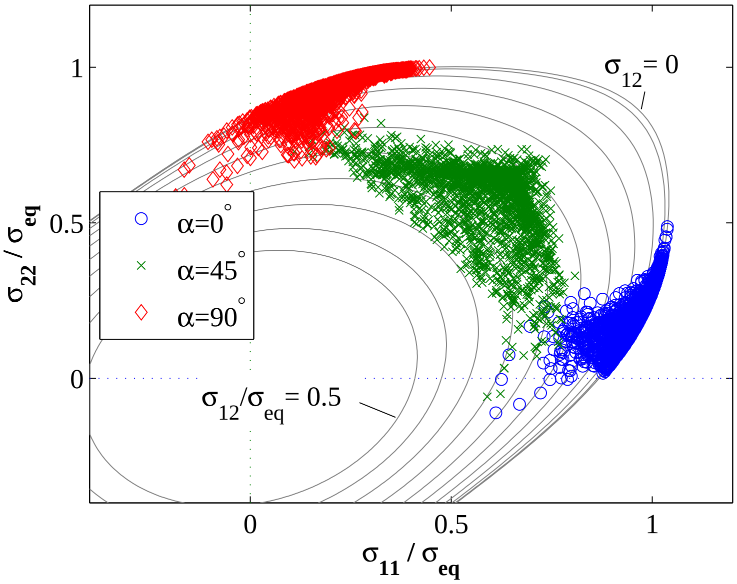

Figure 17: Distribution of the stress states and yield surface using Yld2000-2D

computed tensile force, as in Figure 15. Both models are able to reproduce the experimental force. This shows that such a macroscopic information is not enough to discriminate between models. Table 9 presents the results in terms of Lankford parameter R. In this case, the Yld2000-2D model gives values that are much closer to the experimental ones, obtained from the uniaxial tests. Looking at the cost function for the Yld2000-2D model, it is more than 3 times lower than for the Hill48 model.

It is beyond the scope of this paper to give a complete validation for the Yld2000-2D model, as done for the Hill48 model. This will be the object of future work. However, this simple verification is useful to demonstrate the potentiality of the adopted approach. Another important question, which should be investigated in the future, is if the parameters identified with the

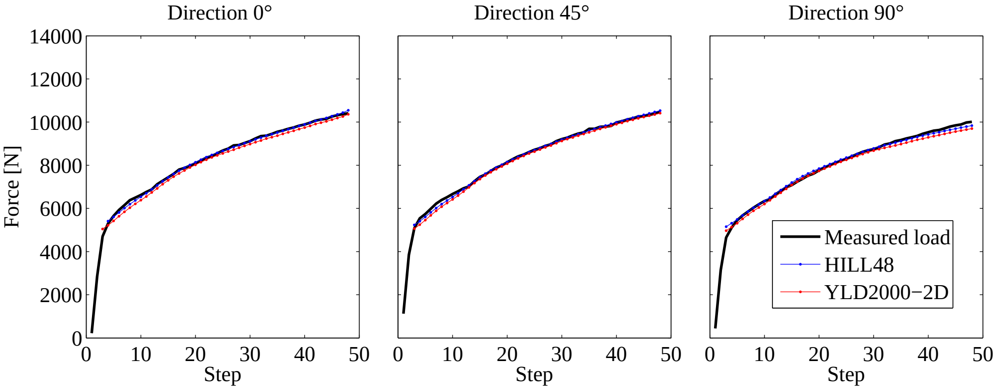

Figure 18: Force comparison with Hill48 and Yld2000-2D

	R_0	R_{45}	R_{90}	Cost function
Hill48	1.21	1.32	1.12	576
Yld2000-2D	2.00	1.63	2.07	153
Reference	1.88	1.54	2.18	

Table 9: Comparison of R values between Hill48 and Yld2000-2D models.

notched specimens are able to predict the plastic behaviour in the biaxial condition. This can be done using a bulge test or a disc compression test, as showed for instance by Tardif and Kyriakides (2012) for the Yld2004-3D model.

6. Conclusion

This paper describes an application of VFM to large strain anisotropic plasticity. A numerical validation was first performed using simulated tests generated according to the Hill48 yield criterion. The procedure led to the identification of the constitutive parameters with a good accuracy using a single test, namely a notched specimen cut at 45° respect to the rolling direction. Then experiments were performed on a stainless steel sheet, using the same specimen geometry. In this case, although the hardening behaviour is well characterized, the procedure was not able to identify the R-values in the different directions. Moreover, in order to have reasonable results, all directions have to be included in the minimization function. Such behaviour can be explained from the fact that the material does not follow the Hill48 model. The VFM provides the Hill48 parameters that best fit the experimental data but these do not match the uniaxial ones. A correct identification of R can be achieved using the Yld2000-2D model.

From this study, the following main outcomes can be listed:

- the experiment should be designed so that, during the test, the stress states in different points of the specimen cover the largest part of the yield surface. In the present application, a notched specimen was used, which produced a rather heterogeneous stress/strain field during deformation. Although satisfactory results were obtained with this geometry, we believe that the specimen design could be improved and further studies are needed in this sense;

- if the material follows the Hill48 plasticity model, a single test is sufficient to correctly identify the parameters; noise can be easily handled with temporal smoothing;
- if the material does not follow the assumed plasticity model, as for the experimental case and the Hill48 model, the method provides the parameters that best fit the experimental behaviour. However, the more heterogeneous the test is, the more difficult it is to find a good compromise. In this case a single test is no more sufficient to identify the parameters;
- the VFM cost function can be used as a benchmark indicator to compare the performance of different constitutive models.

As a general remark, the VFM is an effective tool to study the plastic behaviour of materials at large strains. Full-field data can be processed with low computational times to identify the constitutive parameters of plasticity models. In the future, a more thorough study of the influence of DIC parameters (step size, subset size, virtual strain gauge, etc.) on the identification should be performed, as done by Rossi et al. (2015) for elasticity. More complex constitutive models should be introduced and other specimen shapes should be tested.

Avril, S., Grédiac, M., Pierron, F., 2004. Sensitivity of the virtual fields method to noisy data. Comput. Mech. 34 (6), 439–452.

Avril, S., Pierron, F., Pannier, Y., Rotinat, R., 2008. Stress reconstruction and constitutive parameter identification in plane-stress elasto-plastic problems using surface measurements of deformation fields. Experimental Mechanics 48 (4), 403–419.

Badaloni, M., Rossi, M., Chiappini, G., Lava, P., Debruyne, D., 2015. Impact of experimental uncertainties on the identification of mechanical material properties using DIC. Exp. Mech. Accepted.

Bai, Y., Wierzbicki, T., 2008. A new model of metal plasticity and fracture with pressure and Lode dependence. Int. J. Plasticity 24 (6), 1071–1096.

Banabic, D., Bunge, H.-J., Pöhlandt, Tekkaya, A., 2000. Formability of metallic materials. Springer Berlin.

Barlat, F., Brem, J., Yoon, J., Chung, K., Dick, R., Lege, D., Pourboghrat, F., Choi, S.-H., Chu, E., 2003. Plane stress yield function for aluminum alloy sheets - Part 1: Theory. Int. J. Plasticity 19 (9), 1297–1319.

Barlat, F., Lege, D., Brem, J., 1991. A six-component yield function for anisotropic materials. Int. J. Plasticity 7 (7), 693–712.

Cazacu, O., Plunkett, B., Barlat, F., 2006. Orthotropic yield criterion for hexagonal closed packed metals. Int. J. Plasticity 22, 1171–1194.

Cooreman, S., Lecompte, D., Sol, H., Vantomme, J., Debruyne, D., 2008.

Identification of mechanical material behavior through inverse modeling and dic. Exp. Mech. 48 (4), 421–433.

Coppieters, S., Cooreman, S., Sol, H., Van Houtte, P., Debruyne, D., 2011. Identification of the post-necking hardening behaviour of sheet metal by comparison of the internal and external work in the necking zone. J Mater. Process. Tech. 211 (3), 545–552.

Coppieters, S., Kuwabara, T., 2014. Identification of post-necking hardening phenomena in ductile sheet metal. Exp. Mech. 54 (8), 1355–1371.

Cortese, L., Coppola, T., Campanelli, F., Campana, F., Sasso, M., 2014. Prediction of ductile failure in materials for onshore and offshore pipeline applications. Int. J. Damage Mech. 23 (1), 104–123.

Darrieulat, M., Piot, D., 1996. A method of generating analytical yield surfaces of crystalline materials. Int. J. Plasticity 12, 575–610.

Feigenbaum, H. P., Dafalias, Y. F., 2007. Directional distortional hardening in metal plasticity within thermodynamics. Int. J. Solids Struct. 44, 7526–7542.

Gorry, A., 1990. General least-squares smoothing and differentiation by the convolution (Savitzky-Golay) method. Anal. Chem. 62, 570–573.

Grédiac, M., Hild, F., Pineau, A., 2012. Full-field measurements and identification in solid mechanics. John Wiley & Sons.

Grédiac, M., Pierron, F., 2006. Applying the virtual fields method to the identification of elasto-plastic constitutive parameters. Int. J. Plasticity 22 (4), 602–627.

Gu, X., Pierron, F., 2016. Towards the design of a new standard for composite stiffness identification. Compos. Part A-Appl. S. In press.

Güner, A., Soyarslan, C., Brosius, A., Tekkaya, A., 2012. Characterization of anisotropy of sheet metals employing inhomogeneous strain fields for YLD2000-2D yield function. Int. J. Solids Struct. 49 (25), 3517–3527.

Hill, R., 1948. A theory of the yielding and plastic flow of anisotropic metals. P. Roy. Soc. A-Math. Phy. 193, 281–297.

Kajberg, J., Lindkvist, G., 2004. Characterisation of materials subjected to large strains by inverse modelling based on in-plane displacement fields. Int. J. Solids Struct. 41, 3439–3459.

Kim, J.-H., Barlat, F., Pierron, F., Lee, M.-G., 2014. Determination of anisotropic plastic constitutive parameters using the virtual fields method. Exp. Mech. 54, 1189–1204.

Kim, J.-H., Serpanti, A., Barlat, F., Pierron, F., Lee, M.-G., 2013. Characterization of the post-necking strain hardening behavior using the virtual fields method. Int. J. Solids Struct. 50 (24), 3829–3842.

Lankford, W. T., Snyder, S. C., Bausher, J. A., 1950. New criteria for predicting the press performance of deep drawing sheets. Trans. Am. Soc. Metals 42, 1197–1232.

Le Louëdec, G., Pierron, F., Sutton, M., Reynolds, A., 2013. Identification of the local elasto-plastic behavior of FSW welds using the virtual fields method. Exp. Mech. 53 (5), 849–859.

Lecompte, D., Smits, A., Sol, H., Vantomme, J., Van Hemelrijck, D., 2007. Mixed numerical-experimental technique for orthotropic parameter identification using biaxial tensile tests on cruciform specimens. Int. J. Solids Struct. 44 (5), 1643–1656.

Pannier, Y., Avril, S., Rotinat, R., Pierron, F., 2006. Identification of elasto-plastic constitutive parameters from statically undetermined tests using the virtual fields method. Experimental Mechanics 46 (6), 735–755.

Pierron, F., Avril, S., Tran, V., 2010. Extension of the virtual fields method to elasto-plastic material identification with cyclic loads and kinematic hardening. Int. J. Solids Struct. 47 (22-23), 2993–3010.

Pierron, F., Grédiac, M., 2012. The Virtual Fields Method. Springer, New York.

Rossi, M., Broggiato, G. B., Papalini, S., 2008. Application of digital image correlation to the study of planar anisotropy of sheet metals at large strains. Meccanica 43 (2), 185–199.

Rossi, M., Lava, P., Pierron, F., Debruyne, D., Sasso, M., 2015. Effect of DIC spatial resolution, noise and interpolation error on identification results with the VFM. Strain 51 (3), 206–222.

Rossi, M., Pierron, F., 2012a. Identification of plastic constitutive parameters at large deformations from three dimensional displacement fields. Comput. Mech. 49 (1), 53–71.

Rossi, M., Pierron, F., 2012b. On the use of simulated experiments in designing tests for material characterization from full-field measurements. Int. J. Solids Struct. 49 (3-4), 420–435.

Rossi, M., Sasso, M., Chiappini, G., Amodio, D., Pierron, F., 2014. Performance assessment of inverse methods in large strain plasticity. In: Conf. Proc. Soc. Exp. Mech. Series. Vol. 8. pp. 259–265.

Savitzky, A., Golay, M. J. E., 1964. Smoothing and differentiation of data by simplified least squares procedures. Anal. Chem. 36, 1627–1639.

Sutton, M., Orteu, J.-J., Schreier, H., 2009. Image correlation for shape, motion and deformation measurements. Springer New-York.

Tardif, N., Kyriakides, S., 2012. Determination of anisotropy and material hardening for aluminum sheet metal. Int. J. Solids Struct. 49 (25), 3496–3506.

Teaca, M., Charpentier, I., Martiny, M., Ferron, G., 2010. Identification of sheet metal plastic anisotropy using heterogeneous biaxial tensile tests. Int. J. Mech. Sci. 52 (4), 572–580.

Vegter, H., Van Den Boogaard, A., 2006. A plane stress yield function for anisotropic sheet material by interpolation of biaxial stress states. Int. J. Plasticity 22 (3), 557–580.

Wang, P., Pierron, F., Rossi, M., Lava, P., Thomsen, O., 2016. Optimised experimental characterisation of polymeric foam material using DIC and the virtual fields method. Strain 52 (1), 59–79.

Yoon, J.-W., Barlat, F., Dick, R., Chung, K., Kang, T., 2004. Plane stress yield function for aluminum alloy sheets - Part II: FE formulation and its implementation. Int. J. Plasticity 20 (3), 495–522.